

Reducing object prior-bias from sparse-projection tomographic reconstructions

Preeti Gopal, Sharat Chandran, Imants Svalbe, and Ajit Rajwade

Abstract—Tomographic reconstruction from undersampled measurements is a necessity when the measurement process is potentially harmful, needs to be rapid, or is resource-expensive. In such cases, information from previously existing longitudinal scans of the same object ('object-prior') helps in the reconstruction of the current object ('test') from its significantly fewer measurements. A common problem with these techniques is the influence of object-priors in the reconstruction of new changes in the test. In this work, we mitigate this problem by first estimating the location of changes ('new regions') and then imposing object-prior in *only* those regions which are similar to the prior ('old regions').

Our work is based on longitudinal data acquisition scenarios where we wish to study new changes that evolve within an object over time, such as in repeated scanning for disease monitoring, or in tomography-guided surgical procedures. While reconstruction is easily feasible when measurements are acquired from a large number of projection angles ('views'), it is challenging when the number of views is limited (sub-Nyquist). We show that in the latter case, a 'spatially-varying' technique is appropriate in order to prevent the prior from adversely affecting the reconstruction of new structures that are absent in any of the earlier scans. The reconstruction of new regions is safeguarded from the bias of the prior by computing regional weights that moderate the local influence of the priors. We are thus able to effectively reconstruct both the old and the new structures in the test. We have tested the efficacy of our method on synthetic as well as real projection data, in both 2D and 3D. Our technique significantly improves the overall quality of reconstructions while minimizing the number of measurements needed for imaging in longitudinal studies.

Index Terms—Limited-view tomographic reconstruction, regularization priors, object priors, longitudinal studies.

I. INTRODUCTION

Computed Tomography (CT) deals with the recovery of details of an object's interior from a limited set of projection data acquired by passing X-rays at different orientations ('views'). It is preferable to minimize the radiation exposed in order to prevent any potential damage to it and in order to reduce the acquisition time. Therefore, current research seeks to either significantly reduce the radiation intensity required to reconstruct with adequate fidelity [1], [2], [3], [4] or significantly reduce measurements required to reconstruct with adequate fidelity. For the latter case, there are two lines of pursuit. One is to intelligently choose those sets of projection views that capture most information [5], [6], [7], [8], [9], and the other, which is the focus of this paper, is to design the

Preeti Gopal is currently with the Applied Artificial Intelligence Institute, Deakin University; p.gopal@deakin.edu.au

Sharat Chandran and Ajit Rajwade are with the Department of Computer Science and Engineering, IIT Bombay; {sharat, ajitvr}@cse.iitb.ac.in

Imants Svalbe is with the School of Physics and Astronomy, Monash University; imants.svalbe@monash.edu

reconstruction algorithm in order to achieve the most accurate recovery of the underlying slice, given the measurements from any limited set of views [1], [10], [11].

In conventional data acquisition techniques, tomographic measurements \mathbf{y} are acquired by sampling the physical object \mathbf{x} uniformly with a substantial number of views, ideally above the Nyquist rate. In such a case when there are sufficient measurements, reconstruction using conventional filtered back-projection (FBP) suffices, as seen in Fig. 1 (first column, 800 views). The figure shows the ground truth image (260×260) of naturally growing sprouts at the top left (the details of this dataset are postponed to Section IV).

However, reconstruction from reduced views has been made possible by assuming the data to exhibit certain properties such as smoothness in image space [12], sparsity in gradient space [13] or sparsity under certain mathematical transforms [14], [15] such as the Discrete Cosine Transform (DCT). There are multiple such regularization priors such as the Compressed Sensing based l_1 -ls prior [16]. For the purposes of demonstrating the efficacy of our method, we use the well known Total Variation (TV) regularization prior. If \mathcal{R} represents the acquisition model, then the TV-regularized solution is described by one that minimizes a combination of least squares error and the TV -norm of the object \mathbf{x} . Mathematically, we choose to minimize $J_{TV}(\mathbf{x})$ where

$$J_{TV}(\mathbf{x}) = \|\mathcal{R}\mathbf{x} - \mathbf{y}\|_2^2 + \lambda_{TV} TV(\mathbf{x}) \quad (1)$$

and

$$TV(\mathbf{x}) = \sum_{i,j} \nabla_{ij}(\mathbf{x}), \quad (2)$$

where ∇ represents the gradient operator.

Fig. 1 (second column) demonstrates the benefit of using a regularization prior when the number of projection views is limited (for example reducing sampling to 100 views for the same resolution reconstructed image). We solve this cost function using an optimal first-order method for large-scale TV regularization presented in [17] and available in [18].

When the number of views is reduced significantly further (as discussed in this work), a regularization prior alone is not sufficient. In such cases additional information ('object-prior') specific to the current object being scanned (called the 'test' henceforth) is useful in further improving the reconstruction. While this has been done in the context of dynamic CT-scans (discussed more in Section II), in this paper we use a set S of previous scans of the same object. This is relevant in a longitudinal context: the acquisition of sequential CT scans

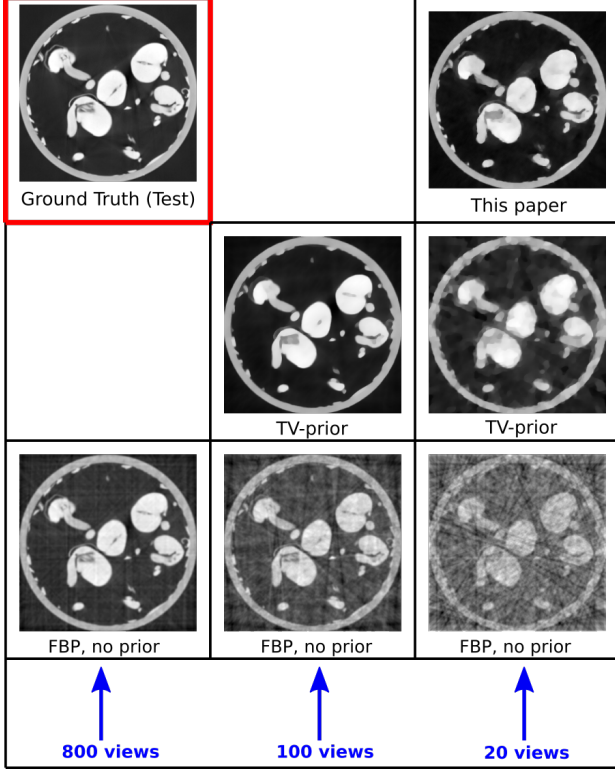


Fig. 1: Illustration of the use of priors in reconstruction as the number of views reduces. For all cases, the ground truth (260×260) appears in the top left. For extremely large number of views (800 views), the standard FBP reconstruction (first column) is of very good quality (Structural Similarity Index Metric, SSIM=0.92, ideal SSIM=1.00). As the number of views become limited (100 views), reconstruction using the Total Variation regularization prior (TV, middle column) is better both visually and quantitatively than FBP (SSIM of 0.96 vs 0.82). If the number of views is drastically reduced (20 views), the presence of both TV prior and object-prior together with the spatially-varying technique of this paper improves the reconstruction (SSIM=0.91) when compared to presence of TV-only prior (SSIM=0.87) or no prior (SSIM=0.64).

of the same subject in order to track time-evolving changes within the subject’s interior.

A. Difficulties

With the use of an object-prior, a *new* challenge emerges. The prior set S may potentially overwhelm the necessary details [19], and when several prior scans are available, finding the best one is an issue. We therefore devise an algorithm that estimates the location and magnitude of new changes in the (unknown) test. As we show in Section V, this prevents the prior from adversely affecting the reconstruction of new regions in the test. We refer to this method as a *spatially-varying* prior-based reconstruction routine, that still uses *all* the previous scans in the set S , without using any of the prior scans *as is*, or endeavoring to choose one “right” prior. In this way, this work is novel and to be contrasted with earlier work. As seen in Fig. 1 (last column, 20 views) our method uses the set S to yield a better reconstruction than the regularization-only, or the backprojection-only methods.

B. Paper organization

This paper is organized as follows. After discussing related work in Section II, Section III lays down the *key contributions* of this work.

Most datasets from commercial scanners do not provide raw measurements. In order to validate our method quantitatively, we created new cone-beam longitudinal CT datasets, details of which are described in Section IV – these will be offered to the community in the public domain. (In addition, Section VI-E1 demonstrates the utility of our method on a longitudinal medical dataset involving the liver in a radio-ablation study.)

We now move to the details. Section V describes the computation of a spatially-varying weights map in order to preserve new changes in the test. Results are presented in Section VI. Section VII discusses tuning of the hyperparameters involved. Finally, we conclude with key inferences that can be drawn from our work in Section VIII.

II. RELATED WORK

The idea of using a reduced number of views is most pronounced in specialized applications. For example, in [12], sparsity-constrained optimization is presented for angiography. Here, the regions of interest are the vessels alone and they are highlighted by physically inserting a contrast agent, and therefore there is an inherent sharper contrast between the vessels and the background. In other applications where the spatial-gradient of the underlying volume is known to be sparse, the ‘total variation’ method, as used in [20], [21], can be applied. However, as shown earlier in Fig. 1, these regularization priors are not sufficient when very few views are acquired, thus needing information from stronger priors such as those obtained from previous scans of the same or similar object.

Most object-prior based reconstruction have been in the areas of dynamic CT and 4D-CT. The object-prior usually consists of an object reconstructed to high quality from a large number of projection angles. One of the earliest pieces of work in this area is the well-cited PICCS method [22] for dynamic CT, which enforces a robust-norm based similarity between the test and the object prior, in addition to a sparsity prior on the test. Its limitation is the unchecked over-emphasis of the prior on the reconstruction of the test at hand. A closely related method called PIRPLE was proposed in [23], with additional steps to register the object prior and the test and a somewhat more flexible combination of data fidelity terms, sparsity prior and object prior. However, this method too has similar limitations as PICCS.

In order to prevent the object-prior from overwhelming the reconstruction of test, a few other approaches have either estimated the motion between the object-prior and the test or have applied very specific object-properties for identifying new changes in test. Examples for the former include [24], where changes across the successive scan volumes are assumed to be continuous, thus enabling the use of optical flow to model the motion between corresponding voxels of different scan volumes. In another study [25], changes between successive scans were modeled by affine deformation whose parameters

were computed for motion-correction, which in turn enables acquisition from fewer views. In [26], all the scan volumes are reconstructed together using spatio-temporal regularization. Here again, the inherent assumption is the continuity across volumes in space or time.

The methods that use object-specific knowledge are [27] and [28]. In [27], knowledge of attenuation coefficient of the fluid is used as a prior for reconstructing its flow through gravel. However, this relies on additional expert domain knowledge which may not be available or which may be infeasible to acquire. Other approaches variously use robust principal components analysis assuming that the object consists of a large static part (background) and a sparse moving part (foreground) [29] or spline-based models for tracking the regions of change in an SIRT framework [30].

All of these techniques [26], [24], [27], [29], [30] essentially reconstruct all the different stages of the object *simultaneously*, and use the extra redundancy across time simultaneously. In the scenario of a longitudinal study (where projection measurements are acquired at instants that are several weeks apart) which we consider in this paper, such approaches are not feasible. A longitudinal study will necessarily require reconstructions soon after acquisition of each set of measurements.

There also exist methods for estimating new changes (in the test) directly in projection space. In such techniques which can be used in longitudinal studies, the object-prior is projected in the same set of views as the current set of test measurements, and a set of projection differences is computed. These projection differences are essentially tomographic projections of differences between the unknown test and the known object-prior. Hence, a variety of reconstruction algorithms can be used to estimate such a difference image which can then be added to the object-prior to yield the final estimate of the test. Such methods have been proposed in [31], [32]. However, reconstruction of the difference image will inherently contain sub-sampling artefacts, and these artefacts will appear in the final reconstruction as there is no mechanism to mitigate them (unlike the method that we propose).

In this paper, we present a technique that makes use of multiple object priors, corresponding to high quality reconstructions of similar objects across time, typically in a longitudinal study. We use these priors to improve the reconstruction of the test from largely undersampled measurements. In particular, we define regions of change between the test and the eigenspace spanned by previous high quality object-priors in a purely data driven manner. Additionally, our technique differentiates between genuine structural changes and “changes” that appear due to undersampling artefacts. Besides this, since we use a statistical model with multiple object-priors, we avoid the problem of selecting an appropriate single object-prior unlike [22], [31], [32], [23], [28] and also make use of the additional information available in multiple priors. Our technique also has the advantage of not requiring any expert-domain knowledge about the object being scanned.

In the recent past, deep learning based techniques have also been widely used for limited view CT reconstruction without the use of any longitudinal object-prior. For example, in [33], a neural network is trained to predict the complete

sinogram from an incomplete one obtained from few-view imaging. This complete sinogram is then fed to analytical reconstruction algorithms to obtain the final reconstruction. Hence, one may in principle use this full sinogram as an alternate initial reconstruction of the test within our framework. [34] presented a cascade of neural networks that predict full-view reconstruction from limited view FBP reconstruction while simultaneously ensuring consistency between the predicted sinogram and the acquired sinogram. [35] trains an adversarial network for artifact removal and edge preservation in limited view reconstruction. While all of the above methods predict full-view reconstruction from the measurements of test object alone, we believe it is beneficial to use information from longitudinal data, especially if naturally available, like in the radio-frequency ablation datasets that we use. In this context, we present an analytical method that uses the available longitudinal data to better inform the reconstruction of the test. We first construct a ‘weights map’ that gives clear insights about regions of change within the object over time.

III. CONTRIBUTIONS

This paper focuses on few-views reconstruction with an emphasis on longitudinal studies. In contrast to the object-prior based studies mentioned above, we reconstruct the current test object without any assumption of continuity of changes or knowledge of the attenuation coefficients of the structures. We also do not make any temporal assumption in terms of time intervals – prior scans could be months apart which is typical in cancer scanning, or could be a few minutes/seconds apart which is typical in CT-guided surgeries. We use the current measurements from few-views and previous scans of the same object.

A key idea in our work is this starting point – the new test volume is close to the space spanned by the eigenvectors of multiple representative previously scanned objects. We then present a method to accommodate new changes in the test that may lie outside of this eigenspace. This will prevent an unnecessary bias when reconstructing the data. As a solution, our method moderates the control of the prior by estimating and imposing spatially-varying weights to the prior in order to reconstruct new structures accurately. This spatially-varying prior tunes the effect of the templates in different regions of reconstruction.

Fig. 2 provides an overview.

In summary, the key contributions are

- We create new 3D biological datasets (Section IV) and present results on real cone-beam projections. Our datasets and code will be made available to the community.
- We design a weights-map to depict the location and strength of new changes in the test at every voxel. A novel algorithm is presented to build this map from sub-sampled measurements of the test and a set of high quality templates. Once the weights-map is built, it is used for accurate reconstruction of those changes in the test that are absent in all of the templates. Results appear in Section VI.

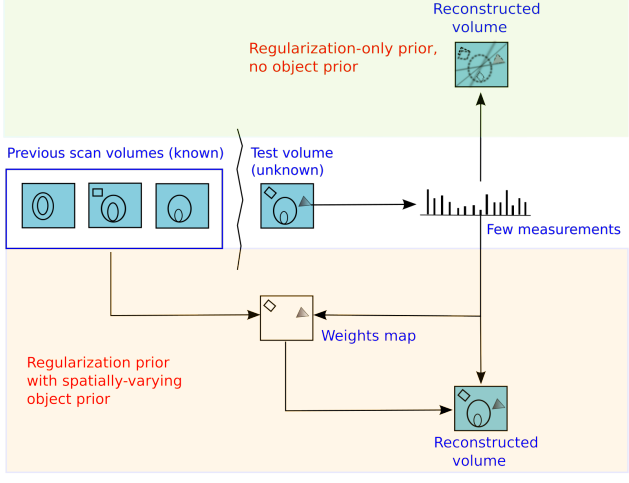


Fig. 2: Overview of our work. (Upper) When the number of measurements is vastly lower than what is conventionally used (last column of Fig. 1) a regularization prior such as Total Variation alone is not sufficient to mitigate the sub-sampling artefacts. (Lower) An object-prior must be used to provide additional information, but in addition, new bias should not be introduced. To this end, here we propose using a spatially-varying weights-map to modulate the effect of object-prior on the final reconstruction.

- We show the efficacy of our results in a real-life medical longitudinal study with data obtained in a clinical setting from a live teaching and research hospital.

While we demonstrate our results with a Total Variation regularization prior, this work provides a technique that can improve upon any chosen baseline reconstruction when measurements are extremely sparse.

IV. DATASETS

In this section, we present details of the biological and medical datasets created and used for this work. For the first two datasets namely, Potato and Okra, the raw measurements and corresponding parameters for cone-beam imaging model are available to us. Hence all reconstructions on these datasets were performed directly from real projection measurements. These datasets are “Type A” datasets in the description below. For the other two datasets (Type B), namely, Sprouts and Liver, the raw measurements and the parameters of imaging model were not available to us (due to propriety concerns) and hence only reconstructed volumes of real data were at hand; we therefore generated measurements from these datasets assuming a circular cone-beam imaging model for 3D and a parallel-beam imaging model for 2D.

In each case, we remark on the design of the choice of the test chosen in the dataset.

A. Datasets with the imaging model available

These consist of longitudinal scans of a Potato and an Okra, both acquired by the first author at the Australian National University (ANU).

Potato: This dataset consisted of four scans of the humble potato (Fig. 3). While the first scan was taken of the

undistorted potato, subsequent scans were taken of the same specimen, each time after drilling a new hole halfway into the potato. Measurements from each scan consisted of real circular cone-beam projections from 900 views, each of size 150×150 . In our experiments, the first 3 volumes were used to build the object-prior and the last volume was used as the test. The ground truth consists of volumes of size $150 \times 150 \times 100$ reconstructed using the Feldkamp-Davis-Kress (FDK) from the full set of 900 projection views.

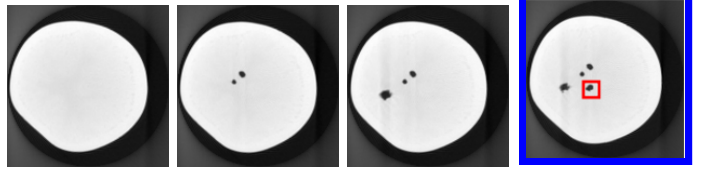


Fig. 3: Potato 3D dataset: One slice each from the scanned objects that are used as templates (the first three from left) and a slice from the test volume (extreme right). Notice the appearance of the fourth hole in the test slice. 3D visualization is available in the supplementary material [36].

Remark: The test slice (unlike the Okra below) was designed to show the presence of a new feature (last picture in Fig. 3). Although the potato is visually bland, paradoxically, this becomes the reason that the Potato is challenging if a new method has to be shown to be effective. Simpler methods may suffice. Nevertheless, we show superior performance with our method by vastly reducing the number of measurements corresponding to the ground truth.

Okra: This dataset is that of an Okra specimen consisting of its five scans (Fig. 4). Each of the scanned volumes consists of a varying number of cuts (or deformations) on the surface of the specimen. The specimen was kept in the same position throughout the acquisitions. Measurements consisted of real circular cone-beam projections from 450 views, each of size 336×156 . In our experiments, the first 4 volumes shown in Fig. 4 were used to build the object-prior and the last volume was used as the test. Note that in the region marked red, all the templates have a deformation, and hence an unchecked reliance of object-prior for the reconstruction of test in this region will result in a deformation. The ground truth consists of volumes of size $338 \times 338 \times 123$ reconstructed using the FDK algorithm [37] from the full set of 450 view projections.

Remark: Unlike the potato, the test was designed as one with the absence of a feature. Although mathematically one is the conjugate of the other, in practice, experimental methods may have difficulties which explains the choice of our test. Notice also that the structure of the Okra is intricate as compared to Potato, and this brings with it a different challenge.

B. Datasets without the imaging model

These consist of longitudinal scans of a portion of a liver obtained from Tata Memorial Centre (TMC) [38] in Parel, Mumbai, and longitudinal scans of Sprouts obtained from Australian National University.

Liver: TMC is the national comprehensive centre for the prevention, treatment, education and research in cancer, and

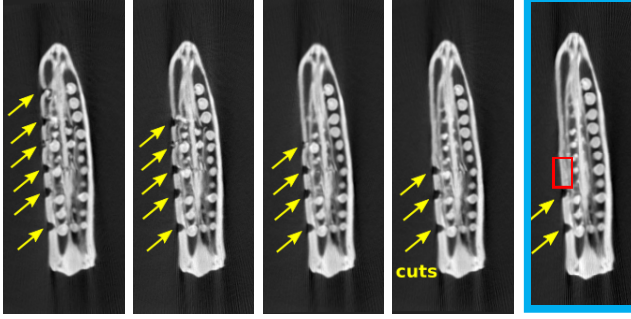


Fig. 4: Okra 3D dataset: One slice each from the scanned objects that are used as templates (the first four from left) and a slice from the test volume (extreme right). Notice the region marked in red box; while all slices have deformities here, the test has none.

is recognized as one of the leading cancer centres in India. The dataset (Fig. 5) from this longitudinal medical study consists of 7 scans taken at different stages of radio-frequency ablation (RFA) study of a liver. In such a procedure [39], the physician inserts a thin needle-like probe into the organ. Repeated CT scans of the patient are acquired in order to track the movement of the needle and to ensure that it is reaching the appropriate target tumor. Once the needle hits the tumor, a high-frequency electric current is passed through the tip of the probe and this burns the malignant tumor (ablation). A fairly high amount of radiation is administered to a patient in this RFA procedure [40], and hence reducing radiation per scan is highly beneficial here.

In our experiments, we generate parallel beam measurements from 2D slices from each of the 7 volumes. Note that all these 7 slices are located at the *same* index (slice number corresponding to the same depth) within each of the respective volumes. Observe (in Fig. 5) that the needle is seen in all of the 7 slices.

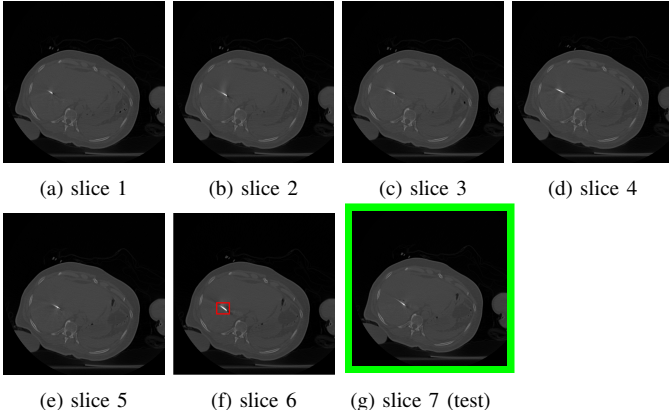


Fig. 5: Radio-frequency ablation dataset: One of the slices (512×512) from each of the 7 scan volumes of a longitudinal study dataset of the liver. Note that in volumes (a) through (g), the needle (shown in red in (f)) approaches the target tumor.

Remark: This dataset is interesting because it comes from a live clinical setting. The oncologist has to be aware of the precise position of the needle contrasted with the site of the

tumor, yet we do not want to create new mutant DNA by further bombarding the patient with X-rays [41].

Sprouts: This dataset consists of six volumes corresponding to six scans of an in-vivo sprout specimen imaged at its various stages of growth (Fig. 6). In our experiments, the first 5 volumes were used to build the object-prior and the last volume was used as the test. The ground truth consists of FDK reconstructed volumes of size $130 \times 130 \times 130$ from a set of 1800 view projections. Test measurements were generated assuming a circular cone-beam imaging model.

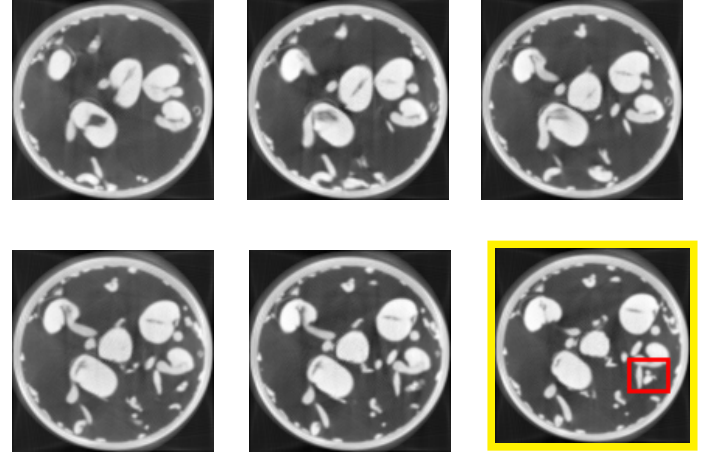


Fig. 6: Sprouts 3D dataset: One slice each from the scanned objects that are used as templates (the first five from left) and a slice from the test (extreme right). One of the many regions in the test that is different from all other templates is the structure within the red box.

Remark: In contrast to the scientific experiment performed for the case of the okra and potato where we introduced man-made defects, the changes in the sprouts here are purely the work of nature. This dataset therefore has a different set of challenges.

V. SPATIALLY-VARYING PRIOR-BASED RECONSTRUCTION

Our method modifies the algorithm presented in [16] and additionally overcomes one of its major limitations by introducing an extra computational step. We first review the eigenspace-cum-CS prior-based reconstruction algorithm which was shown [16] to be better when compared to dictionary-based priors. PCA has been traditionally used to find the significant modes of (Gaussian corrupted) data. In this regard, it has been widely applied in the context of data compression. However, PCA can also be seen as a tool to provide an orthogonal basis to represent the space in which most of the test data could lie (except the new changes). This space is constructed from the available set of previously scanned objects which must cover a realistically representative range of structures.

To begin with, when an object is scanned multiple times, a set of high quality reconstructions (i.e., reconstructions from a dense set of projection views) may be chosen as object-prior for the reconstruction of future scan volumes, which in turn, may be scanned using far fewer measurements. The eigenspace E_{high} of the L previously scanned objects Q_1, Q_2, \dots, Q_L

is pre-computed. Here, it is assumed that most of the test volume, barring the new changes, can be expressed as a sparse linear combination of the principal components (eigenvectors of the covariance matrix) obtained from a group of structurally similar volumes. Hence, the object-prior is represented by means of PCA. For the eigenspace to encompass a range of possible structures in the test slice, the object-prior must represent a wide structural range. Moreover, if these volumes are not aligned, then they must be first registered before computing the prior.

The prior is built by computing the covariance matrix from the template set $\{Q_i\}_{i=1}^L$. The space spanned by the eigenvectors $\{V_p\}_{p=1}^{L-1}$ (eigenspace) of the covariance matrix is the object prior and is assumed to contain most of the test slice (or volume in the case of 3D) that is similar, but not necessarily identical to the object-prior. We use all of the $L - 1$ orthogonal eigenvectors as a basis to represent the unknown test volume. Let μ denote the mean of the previously scanned objects, and α the unknown vector of eigen-coefficients of the test scan, of which α_p is the p^{th} element. Then, once the eigenspace is pre-computed, the test was reconstructed in [16] by imposing a penalty if the estimated slice does not lie within the eigen-space of the object prior. Although such a prior can be very useful in some circumstances, it poses a limitation when we want accurate details of a portion of the new changes. While the object prior compensates very well for the possible artefacts due to sparse measurements, it may dominate the regions with new changes masking the signal.

Ideally, we will want to impose the prior only in the regions that are common between the test and object-prior. Our spatially-varying prior based reconstruction overcomes this limitation by minimizing the following cost function:

$$\begin{aligned} J_3(\mathbf{x}, \boldsymbol{\alpha}) = & \| \mathcal{R}\mathbf{x} - \mathbf{y} \|_2^2 + \lambda_1 TV(\mathbf{x}) + \\ & \lambda_2 \| \mathbf{W}(\mathbf{x} - (\boldsymbol{\mu} + \sum_p V_p \alpha_p)) \|_2^2. \end{aligned} \quad (3)$$

The key to our method is the discovery of a diagonal weights matrix \mathbf{W} , where W_{ii} contains the (non-negative) weight assigned to the i^{th} voxel of the prior. \mathbf{W} is first constructed using some preliminary reconstruction methods, following which Eq. 3 is used to obtain the final reconstruction. In regions of change in test data, we want lower weights for the prior when compared to regions that are similar to the prior.

λ_1 and λ_2 are tunable weights given to the TV-prior and object-prior terms respectively and the specification of these are discussed in Section. VI-B. The unknowns \mathbf{x} and $\boldsymbol{\alpha}$ are solved by alternately minimizing $J_{\boldsymbol{\alpha}}(\mathbf{x})$ using a fixed $\boldsymbol{\alpha}$, and $J_{\mathbf{x}}(\boldsymbol{\alpha})$ using the resultant \mathbf{x} . $J_{\boldsymbol{\alpha}}(\mathbf{x})$ is solved for using an optimal first-order method for large-scale TV regularization presented in [17] and available in [18].

$$\begin{aligned} J_{\boldsymbol{\alpha}}(\mathbf{x}) \triangleq & \| \mathcal{R}\mathbf{x} - \mathbf{y} \|_2^2 + \lambda_1 TV(\mathbf{x}) \\ & + \lambda_2 \| (\mathbf{W}(\mathbf{x} - (\boldsymbol{\mu} + \mathbf{V}\boldsymbol{\alpha})) \|_2^2 \end{aligned} \quad (4)$$

$$J_{\mathbf{x}}(\boldsymbol{\alpha}) \triangleq \| \mathbf{W}(\mathbf{x} - (\boldsymbol{\mu} + \mathbf{V}\boldsymbol{\alpha})) \|_2^2. \quad (5)$$

Solving for $\boldsymbol{\alpha}$ leads to the closed form update:

$$\boldsymbol{\alpha} = [(\mathbf{W}\mathbf{V})^T \mathbf{W}\mathbf{V}]^{-1} \mathbf{V}^T (\mathbf{W}^T \mathbf{W}(\mathbf{x} - \boldsymbol{\mu})) \quad (6)$$

The cost function described in Eq. 3 is biconvex and the convergence of this optimization is guaranteed by the monotone convergence theorem [42].

Computation of weights matrix \mathbf{W} : Since the test is unknown to begin with, it is not possible to decipher the precise regions in \mathbf{x} that are different from all the previously scanned objects ('object-prior'). We start with X^{fdk} , the initial backprojection reconstruction of the test volume using FDK in an attempt to discover the difference between the object-prior and the test volume. Let V_{high} be the eigenspace constructed from high-quality object-prior. However, the difference between X^{fdk} and its projection onto the eigenspace V_{high} will detect the new regions along with many false positives (false new regions). This is because, X^{fdk} will contain many geometric-specific artefacts arising from sparse measurements (angle undersampling), which are absent in the high quality object-prior used to construct the eigenspace V_{high} . To discover unwanted artefacts of the imaging geometry, in a counter-intuitive way, we generate *low quality* reconstruction of the object-prior as described below. The algorithm is discussed next (a simplified version appears as a schematic in the supplementary material and may be used to understand the intuition.)

Algorithm to compute weights-map \mathbf{W} :

- 1) Perform a pilot reconstruction X^{fdk} of the test volume \mathbf{x} using FDK.
- 2) Compute low quality template volumes Y^{fdk} . We assume L previously scanned objects from which we build an eigenspace.
 - a) Generate simulated measurements y_{Q_i} for every template Q_i , using the exact same projections views and imaging geometry with which the measurements \mathbf{y} of the test volume \mathbf{x} were acquired, and
 - b) Perform L preliminary FDK reconstructions of each of the L object-prior from y_{Q_i} . Let this be denoted by $\{Y_i^{\text{fdk}}\}_{i=1}^L$.
- 3) Build eigenspace V_{low} from $\{Y_i^{\text{fdk}}\}_{i=1}^L$. Let P^{fdk} denote projection of X^{fdk} onto V_{low} . The difference between P^{fdk} and X^{fdk} will not contain false positives due to imaging geometry, but will have false positives due to artefacts that are specific to the reconstruction method used. To resolve this, perform steps 4 and 5.
- 4) Project with multiple methods.
 - a) Perform pilot reconstructions of the test using M different reconstruction algorithms like the CS [43] with any suitable sparsity domain such as wavelets (Haar) or DCT, Total Variation [13], Algebraic Reconstruction Technique (ART) [44], Simultaneous Algebraic Reconstruction Technique (SART) [45] and Simultaneous Iterative Reconstruction Technique (SIRT) [46]. Let this set of pilot reconstructions be denoted as $X \triangleq \{X_j^j\}_{j=1}^M$ where

- j is an index for the reconstruction method, and $X^1 = X^{\text{fdk}}$.
- From \mathbf{y}_{Q_i} , perform reconstructions of the template Q_i using the M different algorithms, for each of the L previously scanned objects. Let this set¹ be denoted by $Y \triangleq \{\{Y_i^j\}_{j=1}^M\}_{i=1}^L$ where $Y_i^1 = Y_i^{\text{fdk}}$, $\forall i \in \{1, \dots, L\}$.
 - For each of the M algorithms (indexed by j), build an eigenspace V_{low}^j from $\{Y_1^j, Y_2^j, \dots, Y_L^j\}$.
 - Next, for each j , project X^j onto V_{low}^j . Let this projection be denoted by P^j . To reiterate, this captures those parts of the test volume that lie in the subspace V_{low}^j (i.e., are similar to the template reconstructions). The rest, i.e., new changes and their reconstruction method-dependent-artefacts, are not captured by this projection and need to be eliminated.
 - To remove all reconstruction method dependent false positives, we compute $\min_j(|X^j(x, y, z) - P^j(x, y, z)|)$. (The intuition for using the ‘min’ is provided in the paragraph immediately following step 6 of this procedure.)
 - Finally, the weight to prior for each voxel coordinate (x, y, z) is given by

$$\mathbf{W}_v(x, y, z) = (1 + k(\min_j |X^j(x, y, z) - P^j(x, y, z)|))^{-1}. \quad (7)$$

Note that here $\mathbf{W}_v(x, y, z)$ represents the weight to the prior in the $(x, y, z)^{\text{th}}$ voxel. $\mathbf{W}_v(x, y, z)$ must be low whenever the preliminary test reconstruction $X^j(x, y, z)$ is different from its projection $P^j(x, y, z)$ onto the prior eigenspace, for every method $j \in \{1, \dots, M\}$. This is because it is unlikely that every algorithm would produce a significant artefact at a voxel, and hence we hypothesize that the large difference has arisen due to genuine structural changes. This hypothesis is empirically and quantitatively proven in the next section. The parameter k decides the sensitivity of the weights to the difference $|X^j(x, y, z) - P^j(x, y, z)|$. Selection of k is discussed in detail in Sec. VII.

VI. RESULTS

In this section, we first illustrate the advantage of using multiple types of eigenspaces for the computation of weights map, and then present reconstruction results on all datasets. We show both qualitative and quantitative results. Before we do this, it is import to first consider our method of reporting our results.

A. Metrics

In order to show the efficacy, we will clearly need to have either a gold-standard method, or a ground truth reference reconstruction such as those described in Sec IV (see, for

¹If the set of projection views for every test is fixed a priori, this set of low quality reconstructions can be produced offline and stored, in order to save computational costs. If new sets of projection views for every test are to be allowed, the low quality reconstructions can still be performed efficiently using parallelization.

example, the top left figure in Fig. 1). For quantitative results, we use two metrics: the Root Mean Squared Error (RMSE) and the Structural Similarity Index Metric (SSIM) [47].

RMSE corresponds to error in intensity values and is a measure of absolute error. Our results depend on the optimization library (as mentioned earlier) [18]; however, the range of values returned by other libraries (such as the Matlab implementation of FDK used in our ground truth reconstructions) are not compatible with these. This is not an issue for qualitative results since the display program compensates for range differences. For RMSE, and for purposes of normalization and a fair comparison, while reporting numbers, we therefore rescale intensity values of both the ground truth and the reconstructed results to lie between 0 to 1, so that the best possible RMSE is 0, and the worst value is 1.

On the other hand, SSIM seeks to consider perceptual changes, as well as correlation between adjacent pixels. This can be useful in a clinical context. The SSIM [48] was designed to flexible set coefficients for the following three factors: Structure, Contrast and Intensity. We observed that in many cases, our qualitative results (e.g., when the standard TV regularization method outperforms FDK) do not correspond favourably to the default SSIM settings. We therefore assigned the following coefficients to the factors Structure, Contrast, and Intensity respectively: 0.7, 0.2, 0.1. Our results are optimized for structure-focussed SSIM, but it can be verified that in all cases for the various datasets considered, our results are favourable with either the default metric, i.e., with coefficients 1.0, 1.0, 1.0 or with our structure-focused metric wherein we assign a relatively higher weightage to structure preservation.

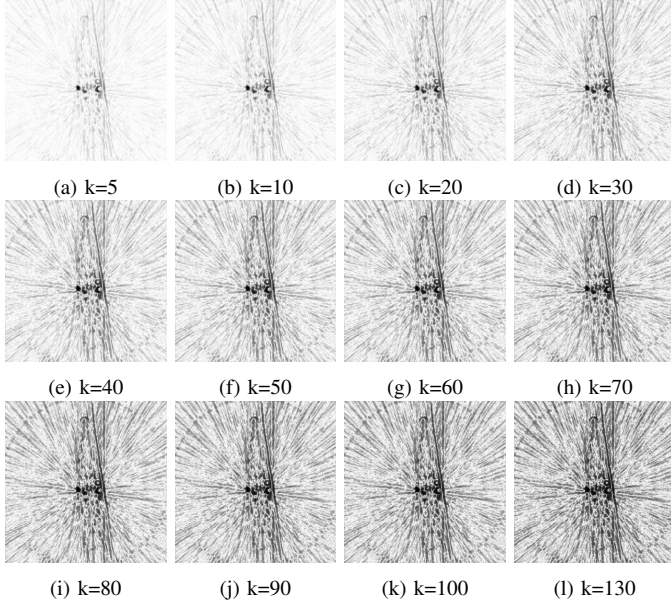
Finally, for a fair comparison in order to not distort metrics, we report these values in what we believe is a reasonable area of “new regions”. In particular, these regions of interest (RoI) are obviously not known in advance, and is thus appropriate for a “test”.

B. Hyper-parameters

Next, we turn to the parameters of the algorithm. λ_1 , λ_2 and k are the three hyper-parameters that need to be chosen carefully for best results. Since the aim of our experiments is to demonstrate the benefit of using weighted prior reconstruction, we proceed to adjust these parameters by (as mentioned earlier) assuming the ground-truth to be known.

Specifically, λ_1 was tuned to maximize the SSIM of the complete reconstructed test volume using the TV-only regularizer. It’s important to note that we retain this value of λ_1 for the spatially-varying prior-based reconstruction, i.e., we do not adjust this value for our spatially-varying method, and, neither do we know the target ROI where the metric is going to be finally employed. With the already chosen optimal λ_1 , we apply our method for a range of λ_2 values and select the one that gives the best SSIM with reference to the ground truth. We note that in practice, however, since ground-truth will never be available, these parameters must be tuned using only the set of templates available. One of the templates can be assumed to be a pseudo-test, and a grid search can be performed to get the best possible hyperparameter values. These values can then be used for reconstructing the ‘real’ test volume.

k defines the sensitivity of the weights map to the difference between test image and object-prior (projection of test onto the space of object-prior). When $k = 0$, our method behaves similar to the reconstruction using TV-only regularization. As k increases, the weights map starts capturing new changes in the test, at the cost of detecting a few false positives i.e., false new changes. In other words, as the weights-map becomes more sensitive to the difference between the test and object-prior, it becomes more noisy. In order to visualize the effect of the hyper-parameter k , we performed 2D reconstructions on okra dataset for different values of k . Fig. 7 shows the weights map obtained for each of the k values and Fig. 8 shows the corresponding final reconstructions. We run our experiments for a few values of k and empirically choose the best reconstruction based on our tolerance for noise in the weights-map. However, when a large number of templates are available, instead of this empirical method, this parameter can be chosen by assuming one of the templates as a pseudo-test and validating the k that results in the best reconstruction (also see Sec 3 of [36]).



Our supplementary material [36] (part-3) discusses an alternate reconstruction method that does not require two of the three hyperparameters: λ_1 and λ_2 . In this method, the computed weights-map is used to stitch parts of the pilot reconstruction and object-prior based on the weights map, and hence there is no optimization to be solved involving λ_1 and λ_2 . The computation of weights map alone requires selection of the hyperparameter value k .

C. Motivation for the use of multiple types of eigenspaces for the computation of weights

The changes and new structures present in the test data will generate different artifacts for different reconstruction techniques. These artifacts would not be captured by reconstructions of the object-prior since the underlying new changes

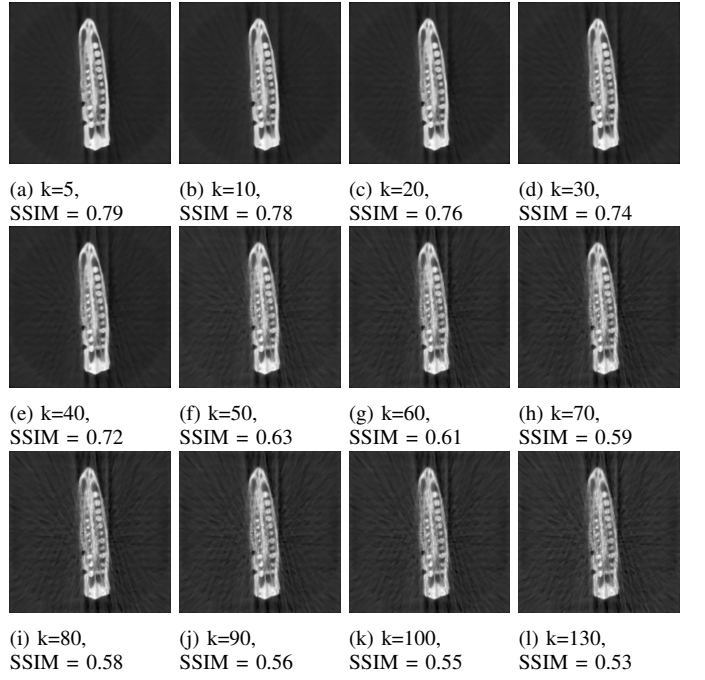


Fig. 8: 2D reconstructions for varying values of k . The SSIM (structure-focussed) values for all images are computed within the red ROI (shown in Fig. 13(a)), the region where the test is different from all of the previously scanned objects.

and structures may be absent in all of the previously scanned objects. We aim to let the weights be independent of the type of artifact. Hence, we use a combination of different reconstruction techniques to generate different types of eigenspaces and combine information from all of them to compute the weights map. To illustrate the benefit of this method, we first performed 2D reconstruction of a test slice from the potato dataset using various reconstruction methods. We used implementations of algebraic methods such as ART, SIRT and SART from [49] and implementations of CS solver from [50]. Among various possible sparsity basis for CS reconstruction, we observed that Haar wavelets and DCT were best suited for this dataset. Fig. 9 shows the test and template slices and Fig. 10 shows the weights maps generated using Eq. 7 by various reconstruction methods. It can be seen that the weights are low in the region of the new change in test data. Because all the iterative methods are computationally expensive, we chose only FBP and TV for computing weights-maps for all 3D reconstructions.

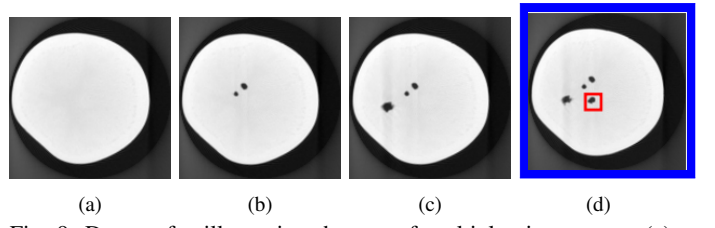


Fig. 9: Dataset for illustrating the use of multiple eigenspaces. (a)-(c): One slice each from the scanned objects, and (d): a slice from the test volume. Notice the appearance of the fourth hole in the test slice.

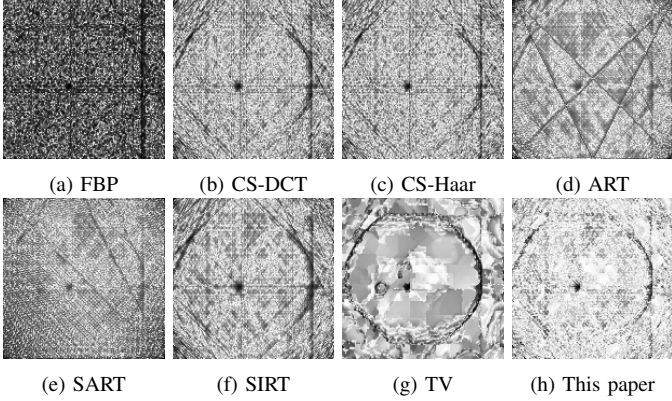


Fig. 10: The motivation for multiple methods is demonstrated with a slice of the data in Fig. 9. The test image in Fig. 9(d) is reconstructed using only 6 views. The weights-maps constructed using different reconstruction methods individually (a)-(g) are inadequate and represent different false positives. By fusing information from all reconstruction methods, as specified in Eq. 7 we get the final weights map (h). The corresponding reconstructions appear in Fig. 11

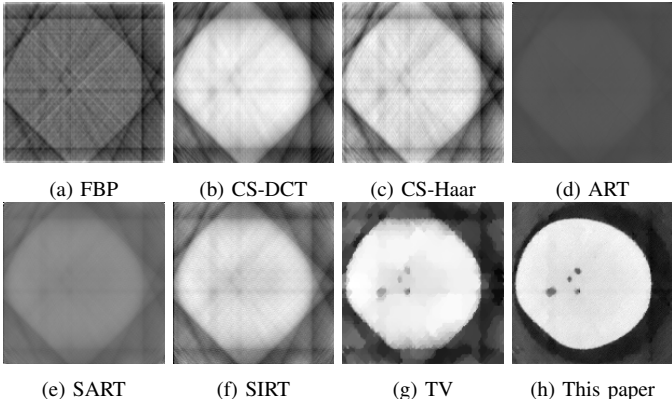


Fig. 11: (a)-(g): Reconstructions of 9(d) from 6 views. The magnitude and sharpness of the artefacts are different for distinct methods. (h) Spatially-Varying-prior method (from this paper) combines weights-map information from all other methods. Quantitative metrics for evaluation of these reconstructions are shown in Table. I.

TABLE I: Default-SSIM ('SSIM-1'), structure-focussed SSIM ('SSIM-2') and RMSE of the reconstructions shown in Fig. 11:(a)-(h).

	(a)	(b)	(c)	(d)	(e)	(f)	(g)	(h)
SSIM-1	0.31	0.48	0.39	0.51	0.55	0.42	0.68	0.78
SSIM-2	0.64	0.72	0.68	0.83	0.81	0.69	0.83	0.88
RMSE	0.38	0.18	0.25	0.43	0.33	0.21	0.11	0.04

D. Reconstruction of datasets with imaging model available

1) **Potato:** The test volume was reconstructed from a partial set of 2% of projection views from which ground truth was reconstructed (see remarks in Sec. IV-A). 2D reconstructions of one of the slices is shown in Fig. 12. A complete 3D reconstruction can be found in the supplementary material [36]. The red ROI spans 7 consecutive slices where the test is different from all of the previously scanned objects.

We observe that our method reconstructs new structures while simultaneously reducing streak artefacts. Table II shows SSIM and RMSE of the reconstructed new regions using

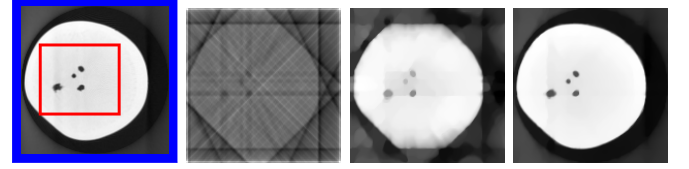


Fig. 12: Reconstruction of potato from 6 projection views—(b) has strong streak artefacts with unclear structure of the potato, (c) largely blurred, and (d) is sharper with significantly reduced streak artefacts.

various methods.

TABLE II: Default-SSIM, structure-focussed SSIM (RMSE) within the ROI of reconstructed potato from various methods. The 2D reconstructed images are shown in Fig. 12, and 3D reconstructed volumes can be seen in [36].

	Backprojection	TV	This paper
2D	0.22, 0.52 (0.36)	0.86, 0.92 (0.06)	0.95, 0.97 (0.03)
3D	0.30, 0.58 (0.26)	0.56, 0.75 (0.21)	0.72, 0.84 (0.16)

2) **Okra:** The test volume was reconstructed from a partial set of 10% of projection views from which ground truth was reconstructed (refer Sec. IV). 2D reconstructions of one of the slices is shown in Fig. 13. A complete 3D reconstruction can be found in the supplementary material [36]. The red ROI spans 7 consecutive slices where the test is different from all of the previously scanned objects. As in the test, the reconstruction by spatially-varying method shows the absence of the deformity and better removal of sub-sampling artefacts when compared to FDK and TV. This is also seen in the SSIM and RMSE values in Table III.

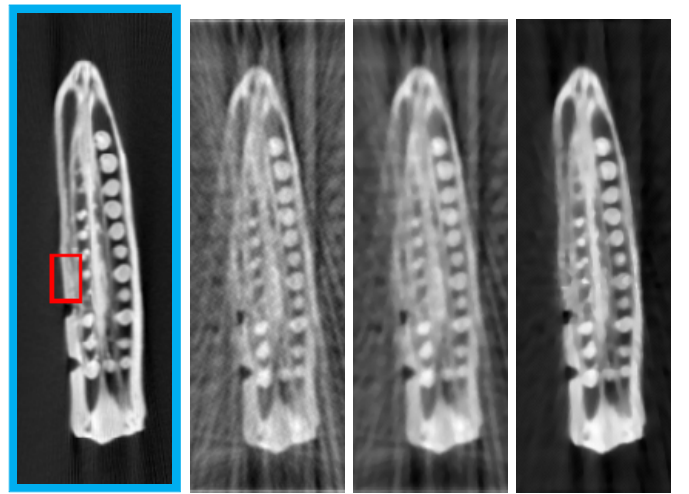


Fig. 13: Reconstruction of okra from 48 projection views (b) has streaky artefacts, (c) has blurred structures and (d) is sharper with significantly less streaky artefacts.

E. Reconstruction of datasets without imaging model

1) **Liver:** Here we show how our technique is useful in a real-life medical longitudinal study. Our data consists of successive scans of the liver taken during a radio-frequency ablation procedure as described in Sec. IV. Our goal is to

TABLE III: Default-SSIM, structure-focussed SSIM (RMSE) within the RoI of reconstructed okra from various methods. The 2D reconstructed images are shown in Fig. 13, and 3D reconstructed volumes can be seen in [36].

	Backprojection	TV	This paper
2D	0.26, 0.46 (0.28)	0.27, 0.50 (0.24)	0.56, 0.74 (0.15)
3D	0.52, 0.65 (0.22)	0.56, 0.70 (0.21)	0.57, 0.71 (0.19)

to track the position of the needle in a relatively stationary background, while simultaneously reducing sub-sampling artefacts. Specifically, we choose slices 1-6 as our object-prior, and reconstruct slice 7 from few-views with the specific goal of tracking the needle and simultaneously reducing artefacts. Fig. 14 shows reconstruction of the test slice from its measurements from only 30 views. The ground truth and reconstructions are quantitatively compared using SSIM and RMSE in Table IV.

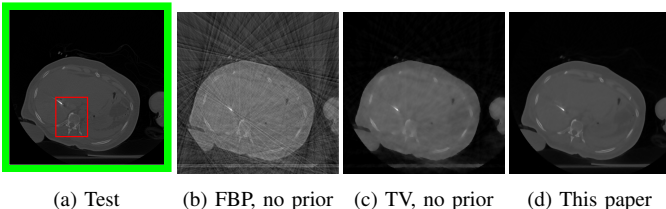


Fig. 14: Reconstruction of ‘test’ (slice 7) from Fig. 5 from only 30 views, using (b) FBP and no prior resulting in streaks (c) TV resulting in blurred bone structures and (d) spatially varying object-prior (slices 1-6 of Fig. 5 are used as object-prior) resulting in clear bone structures with less streaks. The region enclosed in red rectangle is our Region of Interest (RoI) as it contains both the new position of the needle and some background.

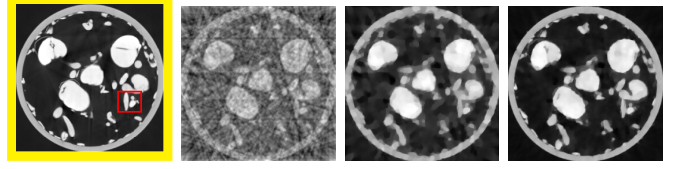
TABLE IV: Default-SSIM, structure-focussed SSIM (RMSE) within the RoI of 2D reconstruction of radio-frequency ablation data of liver from various methods. The reconstructed images are shown in Fig. 14,

	Backprojection	TV	This paper
	0.54, 0.73 (0.04)	0.80, 0.91 (0.09)	0.90, 0.95 (0.03)

2) **Sprouts:** The test volume was reconstructed from a partial set of 1.7% of projection views from which ground truth was reconstructed (refer Sec. IV). The selected 3D ground truth of template volumes, test volume, as well as the 3D reconstructions are shown in the supplementary material [36]. For the sake of exposition, the red region of interest (RoI) has been culled out from 7 consecutive slices in the 3D volume to indicate new structures; other changes can be viewed in the video. 2D reconstruction of one of the slices is shown in Fig. 15. Table V shows the improvement in SSIM and RMSE of the reconstructed new regions as compared to other methods.

TABLE V: Default-SSIM, structure-focussed SSIM (RMSE) within the RoI of reconstructed sprouts from various methods. The 2D reconstructed images are shown in Fig. 15, and 3D reconstructed volumes can be seen in [36].

	Backprojection	TV	This paper
2D	0.42, 0.67 (0.24)	0.61, 0.82 (0.17)	0.72, 0.86 (0.13)
3D	0.44, 0.67 (0.25)	0.47, 0.73 (0.23)	0.66, 0.82 (0.14)



(a) Test (b) FBP, no prior (c) TV, no prior (d) This paper
Fig. 15: Reconstruction of sprouts from 20 projection views (b) has streaky artefacts, (c) has blurred structures and (d) is sharper with significantly less streaky artefacts.

VII. COMPUTATIONAL COMPLEXITY

We discuss the computing burden of our method in two parts: the big-Oh (symbolic) complexity, and the actual time taken on a specific dataset on a specific computer. In the latter case, we provide the actual code [51] for the purposes of reproduction.

1) *Symbolic:* Let

- N denote the number of voxels of test volume,
- L denote the number of templates available,
- M denote the number of pilot reconstruction algorithms used for the computation of weights map, and
- F denote the time taken for optimization. F consists of time taken for alternate minimization of Eq. 3, which in turn consists of time taken for repeated cycles of a closed-form update of α (Eq. 6) and an iterative optimization of x (Eq. 4).

We note that in practice L is independent of N and is likely to be $O(1)$ (e.g., about 12 scans in a year for disease prognosis). Likewise M is also $O(1)$. The speed of the iterative optimization is dependent on the number of imaging views, and is profoundly impacted by the actual numerical optimization technique used. Therefore, the time computational complexity of our method is sum of the following

- 1) $O(NL^2 + L^3)$ for creating eigenspaces, which is, in practice linear, i.e., $O(N)$.
- 2) $O(NLM)$ for deriving weights map, which is, in practice linear, i.e., $O(N)$.
- 3) and the time F taken for iterative minimization, which as mentioned above is not the key contribution of this paper.

In short, the additional burden of the key idea of this paper viz., generating weights map is linear in the number of voxels, although admittedly the burden F of the alternate minimization procedure drives up the cost (as can be seen in Table VI). The supplementary material describes a method to avoid this cost if absolutely necessary.

In terms of space, the complexity is $O(NL + N)$ to store each of the L templates and their low quality reconstructions, and to store one weights map. We only need to store a single weights map volume regardless of the number of templates available.

2) *Example Computation:* If the set of projection views for every test is fixed a priori, a reasonable assumption, the set of low quality reconstructions can be produced offline and stored in order to save computational costs. With this as the basis, Table VI shows the computation times for various stages of

reconstruction of a 2D slice of Liver on MATLAB 2019a on an AMD 2920X 12-Core Processor machine with 64GB RAM.

TABLE VI: Computation times (in seconds) for various stages of reconstruction of a (512×512) 2D slice of Liver from 30 views, on MATLAB 2019a on an AMD 2920X 12-Core Processor machine with 64GB RAM. Our code is available for inspection [51].

FBP	TV	Computation of weights map	Alternate Minimization
0.01	5.63	0.01	34.00

VIII. CONCLUSIONS

This work deals with the effective use of priors for tomographic reconstruction in longitudinal studies. When the number of measurements impedes the benefit of applying classic regularization methods, we discuss the utility of using information from previous scans of the same object, as outlined in Figs. 1 and 2. In order to observe details of new changes accurately, we use a novel spatially-varying prior-based method. This method ensures that the reconstruction of localized new information in the data is not affected by the priors, while the other relatively stationary regions benefit from the extra prior information. We have thus improved state of the art by detecting the strength and location of these regions of change and assigning low prior weights wherever necessary. This innovation becomes evident through the weights maps shown in Figure 10 and the resulting reconstructions shown in Figure 11. The probability of presence of a ‘new region’ is enhanced considerably by a novel combination of different reconstruction techniques. We have validated our technique on medical 2D and real, biological 3D datasets for longitudinal studies. The method is also largely robust to the number of previously scanned objects used. We urge the reader to see the videos of reconstructed volumes in the supplementary material [36].

IX. ACKNOWLEDGMENT

We are grateful to Dr. Andrew Kingston for facilitating data collection at the Australian National University. AR gratefully acknowledges IITB Seed-grant 14IRCCSG012, as well as NVIDIA Corporation for the generous donation of a Titan-X GPU card, which was essential for computing 3D reconstructions for the research reported here. We also thank Dr. Akshay Baheti for providing us with medical data from Tata Memorial Hospital, Mumbai.

REFERENCES

- [1] X. Yang, V. De Andrade, W. Scullin, E. L. Dyer, N. Kasthuri, F. De Carlo, and D. Gürsoy, “Low-dose X-ray tomography through a deep convolutional neural network,” *Scientific Reports*, vol. 8, no. 1, 2018.
- [2] L. Fu *et al.*, “Comparison between pre-log and post-log statistical models in ultra-low-dose CT reconstruction,” *IEEE transactions on medical imaging*, vol. 36, no. 3, pp. 707 – 720, 2016.
- [3] Q. Xie, D. Zeng, Q. Zhao, D. Meng, Z. Xu, Z. Liang, and J. Ma, “Robust low-dose CT sinogram preprocessing via exploiting noise-generating mechanism,” *IEEE Transactions on Medical Imaging*, vol. 36, no. 12, pp. 2487–2498, Dec 2017.
- [4] P. Gopal, S. Chandran, I. Svalbe, and A. Rajwade, “Low radiation tomographic reconstruction with and without template information,” *Signal Processing*, vol. 175, p. 107582, 2020.
- [5] A. M. Kingston, G. R. Myers, S. J. Latham, B. Recur, H. Li, and A. P. Sheppard, “Space-filling X-ray source trajectories for efficient scanning in large-angle cone-beam computed tomography,” *IEEE Transactions on Computational Imaging*, vol. 4, no. 3, pp. 447–458, Sep. 2018.
- [6] A. Cazasnovas, S. Sevestre, F. Buyens, and F. Peyrin, “Statistical content-adapted sampling (SCAS) for 3D computed tomography,” *Computers in Biology and Medicine*, vol. 92, pp. 9 – 21, 2018.
- [7] O. Barkan, J. Weill, S. Dekel, and A. Averbuch, “A mathematical model for adaptive computed tomography sensing,” *IEEE Transactions on Computational Imaging*, vol. 3, no. 4, pp. 551–565, Dec 2017.
- [8] A. Fischer, T. Lasser, M. Schrapp, J. Stephan, and P. B. Noël, “Object specific trajectory optimization for industrial X-ray computed tomography,” *Scientific Reports*, vol. 6, no. 19135, Jan 2016.
- [9] A. Dabravolski, K. J. Batenburg, and J. Sijbers, “Dynamic angle selection in X-ray computed tomography,” *Nuclear Instruments and Methods in Physics Research Section B: Beam Interactions with Materials and Atoms*, vol. 324, pp. 17 – 24, 2014, 1st International Conference on Tomography of Materials and Structures.
- [10] L. L. Geyer, U. J. Schoepf, F. G. Meinel, J. W. Nance, G. Bastarrika, J. A. Leipsic, N. S. Paul, M. Rengo, A. Laghi, and C. N. De Cecco, “State-of-the-art: Iterative CT reconstruction techniques,” *Radiology*, vol. 276, no. 2, pp. 339–357, 2015.
- [11] K. Kilic, G. Erbas, M. Guryildirim, M. Arac, E. Ilgit, and B. Coskun, “Lowering the dose in head CT using adaptive statistical iterative reconstruction,” *American Journal of Neuroradiology*, vol. 32, no. 9, pp. 1578–1582, 2011.
- [12] E. A. Rashed, M. al Shatouri, and H. Kudo, “Sparsity-constrained three-dimensional image reconstruction for C-arm angiography,” *Computers in Biology and Medicine*, vol. 62, pp. 141 – 153, 2015.
- [13] L. I. Rudin, S. Osher, and E. Fatemi, “Nonlinear total variation based noise removal algorithms,” *Physica D: Nonlinear Phenomena*, vol. 60, no. 1, pp. 259–268, 1992.
- [14] D. Donoho, “Compressed sensing,” *IEEE Transactions on Information Theory*, vol. 52, no. 4, pp. 1289–1306, April 2006.
- [15] E. Candès and M. Wakin, “An introduction to compressive sampling,” *IEEE Signal Proc. Mag.*, vol. 25, no. 2, pp. 21–30, March 2008.
- [16] P. Gopal, R. Chaudhry, S. Chandran, I. Svalbe, and A. Rajwade, “Tomographic reconstruction using global statistical priors,” in *DICTA*, Sydney, Nov. 2017.
- [17] T. L. Jensen, J. H. Jørgensen, P. C. Hansen, and S. H. Jensen, “Implementation of an optimal first-order method for strongly convex total variation regularization,” *BIT Numerical Mathematics*, vol. 52, pp. 329–356, 2012.
- [18] Tobias Lindstrøm Jensen and Jakob Heide Jørgensen and Per Christian Hansen and Søren Holdt Jensen, “TV-Regularization Library,” <https://github.com/jakobsj/TVReg>, last viewed–August, 2021.
- [19] Preeti Gopal, “Tomographic Reconstruction: a Radiation Reduction Approach,” Ph.D. dissertation, Indian Institute of Technology Bombay, and Monash University, 2021.
- [20] L. Liu, W. Lin, and M. Jin, “Reconstruction of sparse-view X-ray computed tomography using adaptive iterative algorithms,” *Computers in Biology and Medicine*, vol. 56, pp. 97 – 106, 2015.
- [21] A. G. Polak, J. Mroczka, and D. Wysoczański, “Tomographic image reconstruction via estimation of sparse unidirectional gradients,” *Computers in Biology and Medicine*, vol. 81, pp. 93 – 105, 2017.
- [22] G.-H. Chen, J. Tang, and S. Leng, “Prior image constrained compressed sensing (PICCS): A method to accurately reconstruct dynamic CT images from highly undersampled projection data sets,” *Medical Physics*, vol. 35, no. 2, pp. 660–663, 2008.
- [23] J. W. Stayman, H. Dang, Y. Ding, and J. H. Siewersden, “PIRPLE: A penalized-likelihood framework for incorporation of prior images in CT reconstruction,” *Physics in medicine and biology*, vol. 58, no. 21, pp. 7563–82, Nov 2013.
- [24] K. Ruymbeek and W. Vanroose, “Algorithm for the reconstruction of dynamic objects in CT-scanning using optical flow,” *Journal of Computational and Applied Mathematics*, vol. 367, p. 112459, 2020.
- [25] V. V. Nieuwenhove, “Model-based reconstruction algorithms for dynamic X-ray CT,” Ph.D. dissertation, University of Antwerp, 2017.
- [26] D. Kazantsev, W. M. Thompson, W. R. B. Lionheart, G. V. Eynghoven, A. P. Kaestner, K. J. Dobson, P. J. Withers, and P. D. Lee, “4D-CT reconstruction with unified spatial-temporal patch-based regularization,” p. 447, 2015.
- [27] G. Van Eynghoven, K. J. Batenburg, D. Kazantsev, V. Van Nieuwenhove, P. D. Lee, K. J. Dobson, and J. Sijbers, “An iterative CT reconstruction algorithm for fast fluid flow imaging,” *IEEE Transactions on Image Processing*, vol. 24, no. 11, pp. 4446–4458, 2015.

- [28] M. Heyndrickx, T. D. Schryver, M. Dierick, M. Boone, T. Bultreys, V. Cnudde, and L. V. Hoorebeke, "Improving the reconstruction of dynamic processes by including prior knowledge," *HD-Tomo-Days, Abstracts.*, 2016.
- [29] Z. S. Hao Gao, Jian-Feng Cai and H. Zhao, "Robust principal component analysis-based four-dimensional computed tomography," *Physics in Medicine and Biology*, vol. 56, no. 11, pp. 3181–98, Jun 7 2011.
- [30] V. E. G, B. KJ, and S. J., "Region-based iterative reconstruction of structurally changing objects in CT," *IEEE Trans Image Process.*, vol. 23, no. 2, pp. 909–919, 2014.
- [31] A. Pourmorteza, H. Dang, J. H. Siewersden, and J. W. Stayman, "Reconstruction of difference using prior images and a penalized-likelihood framework," *International Meeting on Fully Three-Dimensional Image Reconstruction in Radiology and Nuclear Medicine*, p. 252–257, 2015.
- [32] J. Lee, J. W. Stayman, Y. Otake, S. Schafer, W. Zbijewski, A. J. Khanna, J. L. Prince, and J. H. Siewersden, "Volume-of-change cone-beam CT for image-guided surgery," pp. 4969–89, Aug 2012.
- [33] R. Anirudh, H. Kim, J. J. Thiagarajan, K. A. Mohan, K. Champliey, and T. Bremer, "Lose the views: Limited angle CT reconstruction via implicit sinogram completion," in *2018 IEEE/CVF Conference on Computer Vision and Pattern Recognition*, 2018, pp. 6343–6352.
- [34] B. Zhou, S. K. Zhou, J. S. Duncan, and C. Liu, "Limited view tomographic reconstruction using a cascaded residual dense spatial-channel attention network with projection data fidelity layer," *IEEE Transactions on Medical Imaging*, vol. 40, no. 7, pp. 1792–1804, 2021.
- [35] D. Hu, Y. Zhang, J. Liu, C. Du, J. Zhang, S. Luo, G. Quan, Q. Liu, Y. Chen, and L. Luo, "SPECIAL: Single-shot projection error correction integrated adversarial learning for limited-angle CT," *IEEE Transactions on Computational Imaging*, vol. 7, pp. 734–746, 2021.
- [36] Supplemental material for 'Reducing object prior-bias from sparse-projection tomographic reconstructions', "in Dropbox," https://www.dropbox.com/sh/ddk0rp15gvaqwgg/AAAddawSnaWqSwaVYB_jVSBUsa?dl=0, Including video reconstruction results.
- [37] L. Feldkamp, L. C. Davis, and J. Kress, "Practical cone-beam algorithm," *J. Opt. Soc. Am.*, vol. 1, pp. 612–619, 01 1984.
- [38] "Tata Memorial Centre," https://en.wikipedia.org/wiki/Tata_Memorial_Centre, Wikipedia.
- [39] J. Dong, W. Li, Q. Zeng, S. Li, X. Gong, L. Shen, S. Mao, A. Dong, and P. Wu, "CT-guided percutaneous step-by-step radiofrequency ablation for the treatment of carcinoma in the caudate lobe," *Medicine*, vol. 94, no. 39, 2015.
- [40] V. Tsapaki, I. A. Tsalaftoutas, C. Triantopoulou, E. Kolliakou, P. Maniatis, and J. Papailiou, "Radiation dose in repeated CT guided radiofrequency ablations," *Phys Med.*, vol. 30, no. 1, pp. 128–31, Feb 2014.
- [41] N. V. Bogdanova, N. Jguburia, D. Ramachandran, N. Nischik, K. Stemwedel, G. Stamm, T. Wernicke, F. Wacker, T. Dörk, and H. Christiansen, "Persistent dna double-strand breaks after repeated diagnostic CT scans in breast epithelial cells and lymphocytes," *Frontiers in Oncology*, vol. 11, p. 1160, 2021. [Online]. Available: <https://www.frontiersin.org/article/10.3389/fonc.2021.634389>
- [42] R. Meyer, "Sufficient conditions for the convergence of monotonic mathematical programming algorithms," *Journal of Computer and System Sciences*, vol. 12, no. 1, pp. 108 – 121, 1976.
- [43] R. Tibshirani, "Regression shrinkage and selection via the Lasso," *Journal of the Royal Statistical Society. Series B (Methodological)*, vol. 58, no. 1, pp. 267–288, 1996.
- [44] R. Gordon, R. Bender, and G. T. Herman, "Algebraic reconstruction techniques (ART) for three-dimensional electron microscopy and X-ray photography," *Theoretical Biology*, vol. 29, no. 3, pp. 471–481, Dec 1970.
- [45] A. Andersen and A. Kak, "Simultaneous algebraic reconstruction technique (SART): A superior implementation of the ART algorithm," *Ultrasonic Imaging*, vol. 6, no. 1, pp. 81 – 94, 1984.
- [46] P. Gilbert, "Iterative methods for the three-dimensional reconstruction of an object from projections," *Journal of Theoretical Biology*, vol. 36, no. 1, pp. 105 – 117, 1972.
- [47] Z. Wang, A. C. Bovik, H. R. Sheikh, and E. P. Simoncelli, "Image quality assessment: from error visibility to structural similarity," *IEEE Transactions on Image Processing*, vol. 13, no. 4, pp. 600–612, April 2004.
- [48] Z. Wang, E. Simoncelli, and A. Bovik, "Multiscale structural similarity for image quality assessment," in *The Thirty-Seventh Asilomar Conference on Signals, Systems Computers, 2003*, vol. 2, 2003, pp. 1398–1402 Vol.2.
- [49] P. C. Hansen and J. S. Jørgensen, "AIR tools II: algebraic iterative reconstruction methods, improved implementation," *Numerical Algorithms*, vol. 79, no. 1, pp. 107–37, Sept 2018.
- [50] K. Koh, S.-J. Kim, and S. Boyd, "l1_ls: Simple matlab solver for l1-regularized least squares problems," https://stanford.edu/~boyd/l1_ls/, last viewed-July, 2016.
- [51] "Code repository for weighted prior reconstruction," <https://github.com/preetigopal/Weighted-Prior-Tomographic-Reconstruction>.